PHYSICAL REVIEW B **110**, 045117 (2024)

Photoinduced insulator-metal transition in paramagnetic $(V_{1-x}Cr_x)_2O_3$

Jiyu Chen,[1] Francesco Petocchi,[2] Viktor Christiansson,[1] and Philipp Werner[1]
[1]*Department of Physics, University of Fribourg, 1700 Fribourg, Switzerland*
[2]*Department of Physics, University of Geneva, 1211 Geneva, Switzerland*

(Received 2 May 2024; revised 30 June 2024; accepted 2 July 2024; published 11 July 2024)

Pump-probe experiments with femtosecond time resolution can be used to disentangle the electronic dynamics from the lattice response and thus provide valuable insights into the nonequilibrium behavior of correlated materials. In Cr-doped V_2O_3, a multiorbital Mott-Hubbard material which has been intensively investigated for decades, time-resolved experiments reported a photoinduced insulator-metal transition leading to a transient metal state with nonthermal properties. Here, we combine nonequilibrium dynamical mean-field theory with realistic first-principles modeling to simulate the ultrafast response of this material to a laser excitation. Our calculations reproduce the insulating initial state, with orbital occupations in agreement with experiment, and reveal an ultrafast pump-induced gap filling associated with a charge reshuffling between the e_g^π and a_{1g} orbitals. However, in contrast to the related compound VO_2, the electronic system thermalizes within a few tens of femtoseconds and we find no evidence for the existence of a metastable nonthermal metal. This suggests that the reported nonthermal behavior in the experiments may be associated with the mismatch between the electronic and lattice temperatures.

DOI: 10.1103/PhysRevB.110.045117

I. INTRODUCTION

Several recent experiments revealed nonthermal metal states in photoexcited insulators, which persist for hundreds of femtoseconds (fs) or even picoseconds (ps) despite a complete gap filling. Examples are $1T$-TaS_2 [1–4], where this behavior has been associated with the excitation of spin-triplet states in strongly coupled bilayers, and VO_2 [5–7], where a theoretical analysis suggested an orbital reshuffling of charge as the origin of the nonthermal properties of the photoinduced metal. A third example is Cr-doped V_2O_3, where pump-probe experiments also reported evidence for a photoinduced metal with long-lived nonthermal electron distributions [8,9].

Vanadium sesquioxide V_2O_3 has been widely studied as a prototype multiorbital Mott-Hubbard system [10–16]. At ambient pressure, V_2O_3 undergoes a metal-insulator transition (MIT) at $T_c \approx 160$ K, associated with a first-order structural transition. Above T_c, the corundum structure hosts a paramagnetic metal (PM) phase, while below T_c, the system exhibits a monoclinic antiferromagnetic insulator (AFI) phase. A different paramagnetic insulator (PI) phase is found at $T > T_c$ by chromium substitution of vanadium [17–19]. This doping-induced first-order metal-to-insulator phase transition from the PM to PI phase is associated with a small discontinuity of the lattice parameter, without a change of lattice symmetry [20,21]. The Cr substitution has often been regarded as equivalent to a negative pressure. However, more recent studies found microscale phase separation in Cr-doped V_2O_3 at ambient pressure and interpreted the Cr atoms as "condensation nuclei" in a percolative PM-PI phase transition, challenging the negative pressure interpretation [16,22].

The high-temperature paramagnetic V_2O_3 system exhibits a corundum crystal structure in which the V^{3+} cations are surrounded by oxygen octahedra. This leads to a $3d^2$electronic configuration of V^{3+}, with empty high energy e_g orbitals and two electrons in the three low energy t_{2g} orbitals. A trigonal distortion of the crystal field further lifts the threefold degeneracy of the t_{2g} orbitals, resulting in one nondegenerate a_{1g} orbital oriented along the c axis and two degenerate e_g^π orbitals oriented predominantly in the hexagonal plane. Furthermore, the vanadium atoms are dimerized by sharing an octahedral surface. This dimerization decreases the energy of the bonding a_{1g} orbital, which becomes partially occupied in the ground state (see Fig. 1).

Polarized x-ray spectroscopy experiments demonstrated that the two valence electrons of V^{3+} form a high spin $S = 1$ state, with an admixture of $e_g^\pi a_{1g}$ and $e_g^\pi e_g^\pi$ configurations [23], suggesting a multiorbital interpretation of the material. Several theoretical studies [10–16] combining *ab initio* calculations in the local density approximation (LDA) [24] with dynamical mean-field theory (DMFT) [25] considered a three-orbital Kanamori-Hubbard description of the system with ($x = 0.038$, PI) and without ($x = 0$, PM) Cr doping. The LDA calculations [26] predict that the Cr doping of V_2O_3 narrows the t_{2g} bandwidth W and thus increases the U/W ratio, which underlies the PM to PI phase transition. The imbalance in the occupation of the a_{1g} and e_g orbitals for both the PI and PM phases is due to the trigonal splitting of the a_{1g} and e_g orbitals. The large Hund's coupling J used in these previous studies favors the high spin state, in agreement with the experiment by Park *et al.* [23].

Recently, the nonequilibrium properties of $(V_{1-x}Cr_x)_2O_3$ have been investigated with multiple time-resolved tools [8,9,27]. By combining time-resolved photoelectron spectroscopy, reflectivity and x-ray diffraction experiments, Lantz *et al.* observed an instantaneous Mott gap collapse in PI $(V_{1-x}Cr_x)_2O_3$ $(x = 0.038)$ after a 35 fs laser pulse

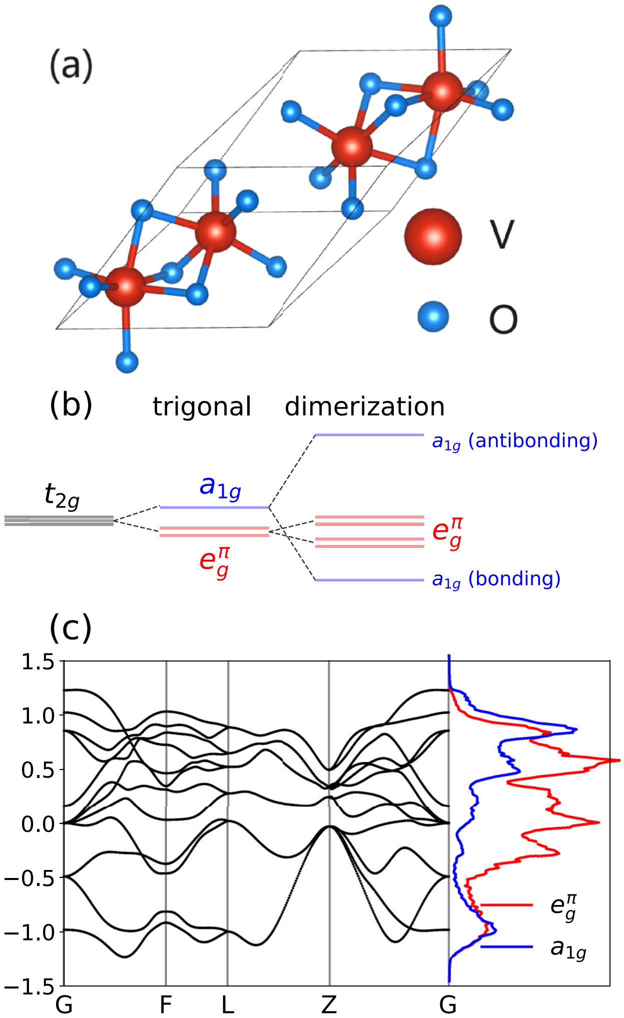

FIG. 1. (a) Lattice structure of V_2O_3, with the four-atom unit cell marked in black. Red spheres: V atoms; blue spheres: O atoms. (b) Energy level scheme of a noninteracting V-V dimer, including the effects of the trigonal crystal field splitting and the V-V dimerization. The six orbitals of each dimer host four electrons. (c) Wannier interpolated band structure (black curves) for PI $(V_{1-x}Cr_x)_2O_3$ ($x = 0.038$). The orbital-projected densities of states are plotted on the right side.

with energy 1.55 eV [8]. They reported the existence of a nonthermal transient metal phase lasting for hundreds of fs and characterized by the overpopulation of the a_{1g} orbital.

Here, we study the photo-induced dynamics in a realistic model of $(V_{1-x}Cr_x)_2O_3$ ($x = 0.038$) using nonequilibrium DMFT [28]. Our three-orbital calculations with *ab initio* derived hopping parameters and realistic interactions yield an equilibrium Mott insulating phase with small gap, as observed in the experiments [9,22]. Nonequilibrium simulations yield a rapid metalization after a photodoping pulse, but also a fast thermalization of the electronic system within a few tens of fs. We will show that both the photoexcitation and the heating result in a significant charge transfer from the e_g^π to the a_{1g} orbitals.

This paper is structured as follows. Section II describes the *ab initio* modeling and the DMFT simulations of the pulse-excited system, Sec. III presents the time-resolved orbital occupations and spectra, while Sec. IV provides a brief discussion and conclusion.

II. MODEL AND METHOD

To derive a realistic model for paramagnetic insulating $(V_{1-x}Cr_x)_2O_3$, we start from the experimental lattice structure for $x = 0.038$ from Ref. [20], perform density functional theory (DFT) calculations using QUANTUM ESPRESSO [29], and downfold to the t_{2g}-like orbitals using WANNIER90 [30]. As in previous equilibrium works [10–16,26] we assume that the small Cr doping only exerts a pressure on the lattice, while the electronic filling is not affected due to charge trapping at the impurity sites. Figure 1(c) shows the Wannier interpolated DFT band structure in the energy range $-1.5 \leqslant \omega \leqslant 1.5$ eV. The e_g^π and a_{1g} bands strongly overlap in this energy range, but the local density of states (DOS) of the a_{1g} orbital is ~0.13 eV higher than for the e_g^π orbitals, due to the trigonal crystal field splitting, as schematically explained in Fig. 1(b). The a_{1g} DOS exhibits a strong bonding-antibonding feature. At the DFT level, the orbital fillings per site are $(a_{1g} : e^\pi_{g1} : e^\pi_{g2}) = (0.56 : 0.72 : 0.72)$.

The time-dependent low-energy Hamiltonian reads

$$\hat{\mathcal{H}}(t) = \sum_{\mathbf{R},\mathbf{R}'}\sum_{i}\Bigg\{\sum_{j}\sum_{\alpha\beta,\sigma} h^{ij}_{\alpha\beta}(\mathbf{R}-\mathbf{R}',t)\, d^{i\dagger}_{\mathbf{R}\alpha\sigma} d^{j}_{\mathbf{R}'\beta\sigma} - \sum_{\alpha\sigma}\mu n^{ai}_{\mathbf{R}\alpha\sigma} + \mathcal{H}^{i}_{\mathrm{K}}(\mathbf{R})\Bigg\},$$

where $\mathbf{R}$ labels the unit cell, $i, j \in \{1, 2, 3, 4\}$ label the V atoms in a given unit cell, $\alpha, \beta \in \{1, 2, 3\}$ label the three t_{2g} orbitals and $\sigma = \{\uparrow, \downarrow\}$ denotes spin. $n_{\alpha\sigma}$ is the occupation per spin of orbital α and μ the chemical potential. The hopping parameters $h^{ij}_{\alpha\beta}(\mathbf{R}, t = 0)$ are extracted from the first-principles calculation. The corresponding bandstructure and DOS are plotted in Fig. 1(c).

We excite the system with a uniform electric field pulse

$$\vec{E}(t) = \vec{E}_0 \sin[\omega_0(t - t_0)]e^{-\frac{(t-t_0)^2}{2\tau^2}} \tag{1}$$

centered at time t_0, with frequency ω_0, peak amplitude E_0, and polarization direction $\hat{E}_0$. The Gaussian envelope with $\tau = 2.6$ fs corresponds to a full width at half maximum (FWHM) of 6.2 fs. The effect of this pulse is to produce time-dependent hopping parameters (Peierls substitution [28])

$$h^{ij}_{\alpha\beta}(\mathbf{R}, t) = h^{ij}_{\alpha\beta}(\mathbf{R}, t = 0)e^{-\frac{ie}{\hbar}\phi_{ij}(\mathbf{R},t)}, \tag{2}$$

with the Peierls phase $\phi_{ij}(\mathbf{R}, t) = -\int_0^t dt'\vec{E}(t') \cdot (\vec{\mathbf{r}}_j - \vec{\mathbf{r}}_i + \mathbf{R})$. Here, $\vec{\mathbf{r}}_i$ is the position of site i.

For the local interaction term, we choose the Kanamori form

$$\mathcal{H}^i_{\mathrm{K}} = \sum_{\alpha} U n^i_{\alpha\uparrow} n^i_{\alpha\downarrow} + \sum_{\alpha\neq\beta} U' n^i_{\alpha\uparrow} n^i_{\beta\downarrow} + \sum_{\alpha<\beta,\sigma} (U' - J) n^i_{\alpha\sigma} n^i_{\beta\sigma} - J \sum_{\alpha\neq\beta} d^{i\dagger}_{\alpha\uparrow} d^i_{\alpha\downarrow} d^{i\dagger}_{\beta\downarrow} d^i_{\beta\uparrow} + J \sum_{\alpha\neq\beta} d^{i\dagger}_{\alpha\uparrow} d^{i\dagger}_{\alpha\downarrow} d^i_{\beta\downarrow} d^i_{\beta\uparrow}, \tag{3}$$

where U is the on-site intraorbital Coulomb repulsion, U' the on-site interaction between different orbitals α and β, and J the Hund coupling. We estimate the interaction parameters using the constrained random-phase approximation (cRPA) [31], where the screening from within the model space is removed, resulting in an effective bare interaction for the model states. The static values obtained with the RESPACK [32] code are $U = 2$ eV and $J = 0.3$ eV, which are substantially smaller than the U = 4–5 eV and J = 0.7–0.9 eV used in previous DMFT studies [10,11,13,14,16]. These static U values neglect the frequency dependence and hence underestimate the correlation effects. We therefore increase the intraorbital interaction to $U = 2.8$ eV to obtain an insulator with a gap size of approximately 0.3 eV, consistent with experiments [9,22].

As the calculated interaction parameters are somewhat smaller than one might expect for V t_{2g}-like states, we have also performed cRPA calculations using the SPEX code [33]. This results in slightly larger values of $U = 3.3$ eV and $J = 0.5$ eV, which, however, are still smaller than the *ad hoc* values chosen in previous theoretical studies. As a side remark, we note that if we include also the unoccupied e_g-like states lying ∼2–3 eV above the Fermi energy into a separate model (a five orbital model for the full V 3d manifold), the cRPA estimates $U_{\text{5-orbital}} = 4.9$ eV and $J_{\text{5-orbital}} = 0.4$–$0.6$ eV become close to the values used in the literature. But these interaction parameters are not the appropriate ones for the three-orbital model considered in our calculations.

We employ nonequilibrium DMFT [28,34] to compute the evolution of the laser-excited lattice system. Similarly to the equilibrium version, the lattice is mapped to a quantum impurity problem with a self-consistently determined bath. The only difference is that in the nonequilibrium case, all the quantities are defined on the Kadanoff-Baym contour $\mathcal{C}$ [28]. The impurity action takes the form

$$S_{\text{imp}} = -i\int_{\mathcal{C}} dt\, \mathcal{H}_{\text{K}}(t) - i\int_{\mathcal{C}} dt\, dt' \sum_{\alpha,\sigma} d^{\dagger}_{\alpha,\sigma}(t)\Delta_{\alpha,\sigma}(t,t')d_{\alpha,\sigma}(t), \qquad (4)$$

with $\mathcal{H}_{\text{K}}$ the local interaction Hamiltonian defined in (3) and $\Delta_{\alpha,\sigma}(t,t')$ the hybridization function describing the exchange of electrons between the impurity and the bath. As in previous materials studies, we employ real-space DMFT calculations with a simplified self-consistency [4,7,35], which allows us to circumvent the explicit calculation of the lattice self-energies and lattice Green's functions. The hybridization function is obtained from the local (impurity) Green's functions $G_{\alpha,\sigma}(t,t')$ as

$$\Delta_{i,\alpha,\sigma}(t,t') = \sum_{j,\beta} h^{ij}_{\alpha\beta}(t)G_{j,\beta,\sigma}(t,t')h^{ji}_{\beta\alpha}(t'), \qquad (5)$$

where the site index i takes the values $\{1, 2, 3, 4\}$, since we separately solve four impurity models corresponding to the four atoms within one unit cell. For each impurity i, the index j ranges over all the remaining sites of the lattice.

For the calculation of $G_{\alpha,\sigma}(t,t')$, we employ a noncrossing approximation (NCA) impurity solver [36,37]. This method introduces pseudoparticle Green's functions and pseudoparticle self-energies for each of the $3^4 = 64$ local impurity states, and solves coupled pseudoparticle Dyson equations with a first-order-in-Δ approximation to the pseudoparticle self-energies. This method is expected to produce qualitatively correct results for the nonequilibrium dynamics in Mott insulating systems. A detailed description of the NCA solver and some benchmarks can be found in Ref. [37].

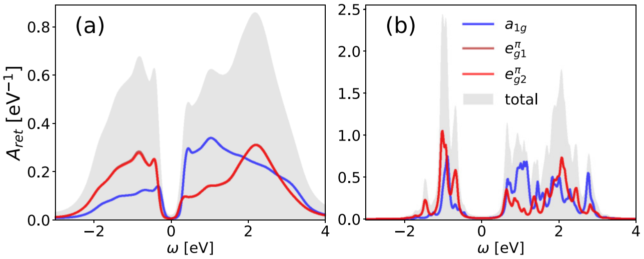

FIG. 2. Orbital-resolved and total spectra in equilibrium obtained with DMFT (a) and ED (b). Both calculations yield a gap.

The initial temperature in our calculations is $T = \frac{1}{12}$ eV. (Room temperature is too low for the NCA solver, but we do not expect qualitative differences due to the 0.3 eV gap.) To help with the interpretation of the spectra, we also solve the isolated dimer system using exact diagonalization (ED).

III. RESULTS

A. Equilibrium system

We first discuss the equilibrium spectra obtained from DMFT and ED. As shown in Fig. 2(a), the DMFT spectrum has a gap of 0.3 eV and the spectral weight below the Fermi energy is contributed by all three t_{2g} orbitals. In the interacting system, the relative occupations of the orbitals are $(a_{1g} : e^{\pi}_{g1} : e^{\pi}_{g2}) = (0.38 : 0.81 : 0.81)$, in good agreement with the results of polarized x-ray spectroscopy experiments, which reported the ratios (0.4 : 0.8 : 0.8) [23]. Similar results were also obtained in the previous LDA+DMFT studies [10,11,13–16].

The ED spectrum of a single dimer with the same interaction and intradimer hopping parameters is shown in Fig. 2(b). Based on the ED analysis, we identify an almost degenerate group of nine low-energy states ("ground states"). Within a V-V dimer, the intersite hopping between two a_{1g} orbitals is 0.39 eV while the hopping amplitudes between the e^{π}_{g} orbitals are much smaller, consistent with the results reported in Ref. [26]. Thus, the ground state manifold is essentially given by the product of two local spaces with occupation $e^{\pi}_{g1}e^{\pi}_{g2}$ and spin $S = 1$ (one for each site). Here and in the following, "ab configuration" refers to a state with one electron in the a orbital and one electron in the b orbital, on the same site. Only 0.03 eV higher in energy, there exists another group of nine states with mixed $e^{\pi}_{g1}e^{\pi}_{g2}$ and $e^{\pi}_{g}a_{1g}$ configuration. Even though at the LDA level the trigonal spitting pushes the a_{1g} bonding orbital below the e^{π}_{g} orbitals, in the presence of interactions the high-spin configurations with two electrons in the e^{π}_{g} orbitals are preferred. The 0.03 eV gap between the two groups of low energy states corresponds roughly to room temperature and explains the experimentally observed occupation of both the $e^{\pi}_{g1}e^{\pi}_{g2}$ and $e^{\pi}_{g}a_{1g}$ states [23].

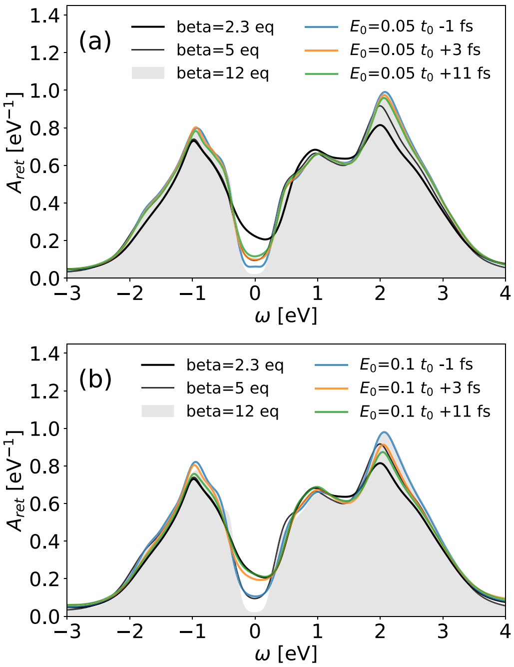

FIG. 3. Total equilibrium (eq) spectra for different temperatures (black or gray) and nonequilibrium spectra after the pulse excitation with $\omega_0 = 2.7$ eV (colored lines). Panel (a) is for pulse amplitude $E_0 = 0.05$ V/Å and panel (b) for $E_0 = 0.1$ V/Å.

Combining the results from the DMFT and ED calculations, we conclude that the *ab initio* modeling of Cr-doped V_2O_3 yields a strongly correlated insulating material, whose electronic structure (gap size and Hubbard band features) is shaped by the local multiorbital interactions. As we will see later, the large number of nearly degenerate low-energy states in our model has significant effects on the nonequilibrium dynamics.

The temperature dependence of the DMFT spectra is shown by the gray shading and black lines in Fig. 3. Here, β is the inverse temperature in eV^{-1}, so that $\beta = 2.3$ eV^{-1} corresponds to $T \approx 5000$ K. We can see that an electronic temperature of several thousand K, as expected after a pump excitation, leads to a significant filling of the gap.

B. Pulse-excited system

We first search for the polarization direction $\hat{E}_0 = \vec{E}_0/|E_0|$ and pump frequency ω_0 which yields the maximum energy absorption and then simulate the time evolution using nonequilibrium DMFT. The polarization angle θ between $\hat{E}_0$ and the dimerization axis $\mathbf{c}_R$, as well as the laser frequency ω_0 are varied in the relevant range, and the resulting energy absorption is shown in Fig. 4. Both in the DMFT and ED simulations, $\theta = 0^\circ$ maximizes the absorption. With this polarization fixed, the DMFT simulations predict a broad energy absorption peak with a maximum corresponding to the pulse frequency $\omega_0 = 2.7$ eV; see the red curve in Fig. 4(a). In the ED analysis of the dimer, the energy absorption spectra strongly depend on the temperature (see blue lines). As discussed before, the ground state mainly involves high-spin $e_{g1}^{\pi}e_{g2}^{\pi}$ configurations. Therefore, the laser excitation of the ground state creates doublons in the e_g^{π} orbitals, i.e., configurations where one of the e_g^{π} orbitals is occupied by two electrons with spin up and spin down,

$$\left(e_{g1}^{\pi\uparrow}e_{g2}^{\pi\uparrow}\right)_A + \left(e_{g1}^{\pi\downarrow}e_{g2}^{\pi\downarrow}\right)_B \rightarrow \left(e_{g1}^{\pi\uparrow}\right)_A + \left(e_{g1}^{\pi\downarrow}e_{g2}^{\pi\uparrow\downarrow}\right)_B,$$

at the cost of $U = 2.8$ eV (here A and B are the two atoms in a dimer). At high temperature, the thermal state includes both $e_{g1}^{\pi}e_{g2}^{\pi}$ and $e_g^{\pi}a_{1g}$ configurations, which activates additional excitations with energy $U - 3J = 1.9$ eV, given for example by

$$\left(e_{g1}^{\pi\uparrow}e_{g2}^{\pi\uparrow}\right)_A + \left(e_{g1}^{\pi\uparrow}a_{1g}^{\uparrow}\right)_B \rightarrow \left(e_{g1}^{\pi\uparrow}\right)_A + \left(e_{g1}^{\pi\uparrow}e_{g2}^{\pi\uparrow}a_{1g}^{\uparrow}\right)_B,$$

and with energy $U + 2J = 3.4$ eV, for example

$$\begin{aligned}&\left(e_{g1}^{\pi\uparrow}e_{g2}^{\pi\uparrow}\right)_A + \left(e_{g2}^{\pi\downarrow}a_{1g}^{\downarrow}\right)_B\\ &\quad\rightarrow \left(e_{g1}^{\pi\uparrow}\right)_A + \left(\alpha e_{g1}^{\pi\downarrow}e_{g2}^{\pi\uparrow\downarrow} + \gamma e_{g2}^{\pi\downarrow}a_{1g}^{\uparrow\downarrow}\right)_B,\end{aligned}$$

similar to the three-band Kanamori-Hubbard model in the atomic limit with degenerate orbitals [38]. We conclude that the multiorbital interactions play a crucial role in the photoexcitation process. The initial temperature of the system is also important, because it controls the initial state population and influences the charge dynamics.

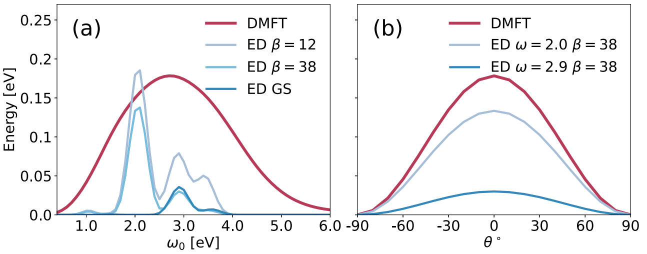

FIG. 4. (a) Energy absorption as a function of the pulse frequency ω_0 with $\theta = 0^\circ$. (b) Energy absorption as a function of the polarization angle with frequency $\omega_0 = 2.7$ eV. $\theta = 0^\circ$ corresponds to a polarization along the dimer, in the $\mathbf{c}_R$ direction.

With the insights from the ED analysis on the laser-induced doublon creation, we now investigate the reshuffling and decay of the excited doublons in the infinite-size system using DMFT. The DMFT results for the time-dependent orbital occupations are shown in Fig. 5(a). In this study, we perform single-site DMFT calculations (in contrast to the cluster DMFT calculations of Ref. [7]) and report the population dynamics for a single V atom. These calculations assume that the spin orientations on neighboring sites are uncorrelated, i.e., they neglect possible short-ranged antiferromagnetic correlations. Doublon production by nearest-neighbor hopping is possible if the spins in the two involved orbitals are oppositely oriented.

During the pulse, which reaches its maximum at $t = t_0 = 6.6$ fs (indicated by the red vertical line), the t_{2g} electrons are driven back and forth between the vanadium atoms, as can be deduced from the oscillations of the occupations on a given site. This charge sloshing, and other effects of the laser pulse like bandwidth renormalization [39,40], also lead to a modulation in the double occupation, as seen by the oscillating doublon density in Fig. 5(b). We note that the DMFT simulation represents an infinite bulk system and

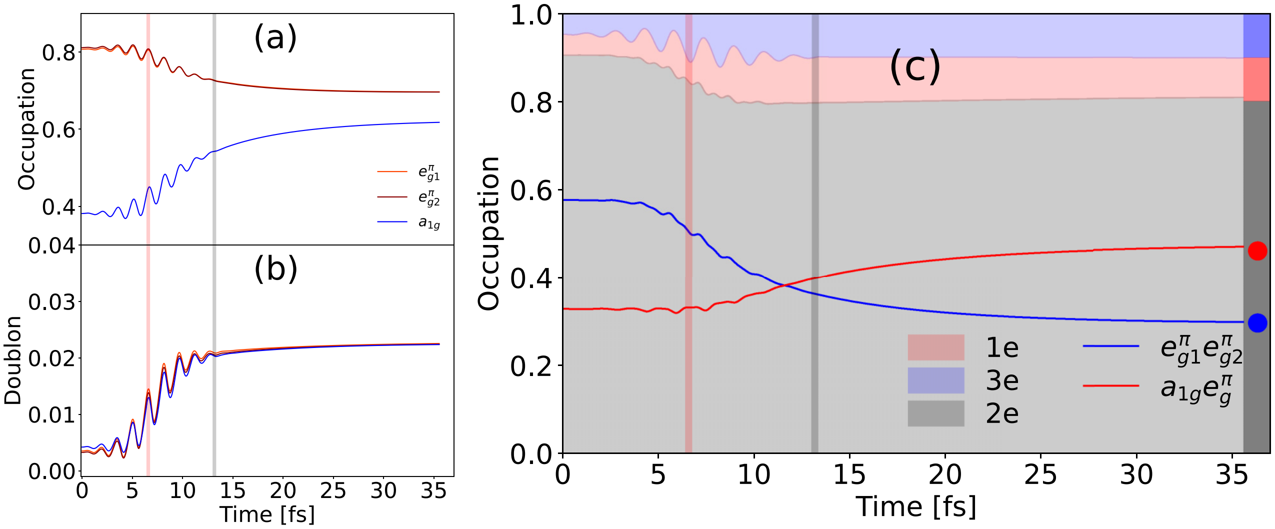

FIG. 5. Occupation (a) and double occupation (or doublon density) (b) in each of the three orbitals, for a given vanadium atom. (c) Projection of the state occupation onto electron number sectors (colored shadings), for a given vanadium atom. Within the $n = 2$ sector, the states are further projected onto the indicated orbital configurations. The red and gray vertical lines indicate the maximum and the end of the laser pulse, respectively. The colored bars and dots at the right side of the panel indicate the weights of the charge sectors and the weights of the $e^{\pi}_{g1}e^{\pi}_{g2}$ and $e^{\pi}_{g}a_{1g}$ configurations in the thermalized state (equilibrium system with the same energy as the system after the excitation).

captures interaction and heating effects, i.e., the conversion of the injected energy into various electronic excitations. Figure 5 reveals a significant rearrangement of charge between the different orbitals. In particular, panel (a) shows a significant flow of charge from the e^{π}_{g} to the a_{1g} orbitals during the pulse, which ends approximately at 13 fs (grey vertical line), followed by a slower reshuffling and saturation around 35 fs. The average doublon density increases during the pulse, but remains low.

As illustrated in Fig. 5(c), in the equilibrium PI phase, the sector with $n = 2$ electrons (gray shading) represents more than 90% of the weight of the initial state. The laser pulse mainly reshuffles the states within this $n = 2$ sector, but also produces some states with $n = 1$ and $n = 3$ through charge excitations between vanadium atoms. These charge excitations are indicated by the red and violet shading. After the end of the pulse ($t \gtrsim 13$ fs), the weight of the $n = 2$ sector remains almost unchanged, and in our closed system (without energy dissipation to phonons or other external degrees of freedom), the electrons are expected to thermalize at $T \approx 5000$ K. This is the temperature at which the energy of the equilibrium system equals the energy of the simulated system after the pulse. The corresponding weights of the charge sectors and the weights of the $e^{\pi}_{g1}e^{\pi}_{g2}$ and $e^{\pi}_{g}a_{1g}$ configurations are indicated by the colored bars and dots at the right side of panel (c). Within the two-electron sector, the $e^{\pi}_{g1}e^{\pi}_{g2}$ configurations of the ground state manifold dominate the PI phase in equilibrium. During and after the pulse, the weight of these configurations decreases rapidly, while the weight of the $a_{1g}e^{\pi}_{g}$ states increases rapidly, consistent with panel (a). After the pulse, the $a_{1g}e^{\pi}_{g}$ configurations become dominant.

The above observations imply that during each cycle of the laser pulse, a large fraction of the created doublons and holons ($n = 3$ and $n = 1$ sectors) recombines back to the $n = 2$ sector, but possibly into different orbitals than before the pulse. The switching of the $e^{\pi}_{g1}e^{\pi}_{g2}$ and $a_{1g}e^{\pi}_{g}$ populations shows that electrons flow from the e^{π}_{g} orbitals to the a_{1g} orbital. The rapid decay of the doublons indicates that the lifetime of potential nonthermal transient states in Cr-doped V_2O_3 is very short. Indeed, the weights of the different charge sector configurations are very close to the thermal reference values already 20 fs after the pulse, and there is no indication of a trapping in a nonthermal transient state. This is in contrast to the finding for the related material VO_2 in Ref. [7], where, due to the V^{4+} configuration, there is one electron in the three t_{2g} orbitals and where the much stronger dimerization locks this electron in the lowest lying bonding orbital, well separated from other states.

The population of the $a_{1g}e^{\pi}_{g}$ states generates spectral weight in the gap region and results in the rapid partial gap filling seen in Fig. 3(b). Our calculations thus demonstrate that the metallic phase observed after photodoping is a consequence of the charge reshuffling between e^{π}_{g} and a_{1g} orbitals. But also the nonequilibrium spectrum after the pulse is very similar to a thermal spectrum corresponding to a high electronic temperature ($\beta \approx 2.3\ \mathrm{eV}^{-1} \leftrightarrow T \approx 5000$ K), see the comparison to the thermal results (black gray curves).

In Fig. 6, we present the time-dependent DMFT spectra, obtained for the optimal polarization ($\theta = 0^\circ$) and absorption frequency ($\omega_0 = 2.7$ eV) as well as the typical laser frequency in photodoping experiments [8,9] ($\omega_0 = 1.55$ eV). The total spectral functions A^{ret}, electron occupation functions $A^{<}$, and hole occupation functions $A^{>}$ are shown for probe time $t_0 = 17$ fs and two pulse amplitudes. These spectra are obtained from the imaginary parts of the corresponding energy-dependent Green's functions, which we calculate using the Wigner

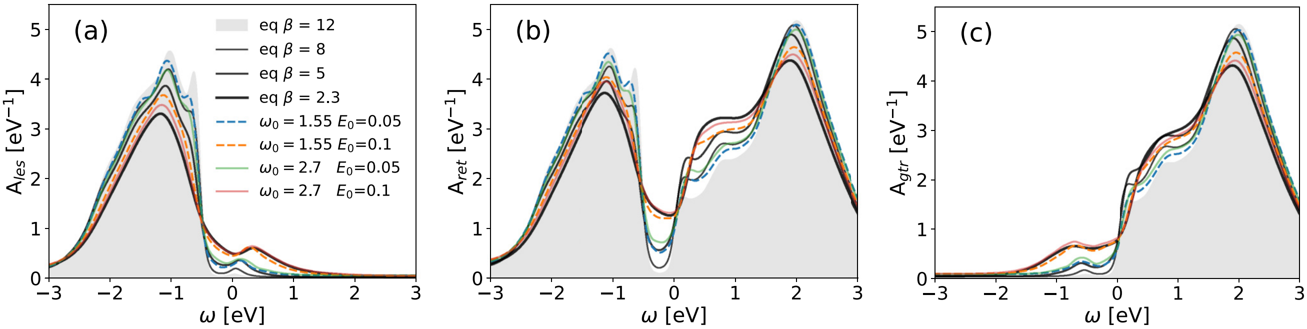

FIG. 6. Local lesser (a), retarded (b) and greater (c) spectra obtained with DMFT in equilibrium for different temperatures (gray shading and black lines) and 17 fs after the pulse excitation for the indicated E_0 (V/Å) and ω_0 (eV). The initial inverse temperature is $\beta = 12$ eV^{-1}.

transformation [28]

$$G^X(\omega, t_{\rm av}) = \int dt_{\rm rel} e^{i\omega t_{\rm rel}} G^X(t, t'). \tag{6}$$

Here, $t_{\rm rel} \equiv t - t'$ is the relative time, $t_{\rm av} \equiv t + t'$ is the averaged time, and X refers to the retarded, lesser and greater components of the contour Green's function. $A^<(\omega, t_{\rm av})$ approximately represents the time-resolved photoemission spectrum. For both pulse frequencies, the laser excitation results in a partial filling of the gap, which is slightly more pronounced for the higher energy excitation (since the larger amount of injected energy results in stronger heating).

In Fig. 7 we plot the difference between the nonequilibrium occupation at $t = 17$ fs and the initial equilibrium occupation for $\beta = 12$ eV^{-1} (green, orange, and blue lines), as well as differences between higher-temperature equilibrium occupations and the initial occupation (black lines). Panel (a) is for the $\omega_0 = 2.7$ eV pulse and panel (b) for the $\omega_0 = 1.55$ eV pulse. Consistent with the previous observations, we find that the nonequilibrium occupation at $t = 17$ fs is almost thermalized (see data for $\omega_0 = 2.7$ eV, where the thermalized system has $\beta = 2.3$ eV^{-1}). Comparing our results to Fig. 2(b) of Ref. [8], we see that their difference ΔI in photoemission spectra between the pumped and unpumped systems looks qualitatively similar for the shortest reported delay time of 50 fs [41]. We note that since the initial system is insulating, the location of the Fermi energy could be somewhat different in the experiment, which may explain the horizontal shift between the theoretical and experimental curves.

On a timescale of several hundred fs, ΔI vanishes inside and above the gap region, while after 2 ps it approaches a distribution consistent with a slightly increased equilibrium temperature. In view of our simulation data, which show no evidence for a delayed thermalization in the electronic system, these experimental results are most naturally interpreted in terms of a two-temperature picture [42,43], where the hot electrons couple to the lattice and cool down on a ps timescale.

IV. CONCLUSIONS

Our *ab initio* nonequilibrium DMFT simulations of Cr-doped V_2O_3 clarified the photoinduced charge dynamics during and after a laser pulse applied to the PI phase. The optical excitation induces an ultrafast gap filling by generating interorbital electron pairs, which thermalize within tens of fs to a high-temperature metallic state. On a longer timescale, the lattice is expected to cool down the electronic system, and an explicit simulation of this energy reshuffling would require the introduction of phonon degrees of freedom. For the short-time dynamics, our study shows that multiorbital Mott and Hund physics play a key role in the formation of dominant $S = 1$

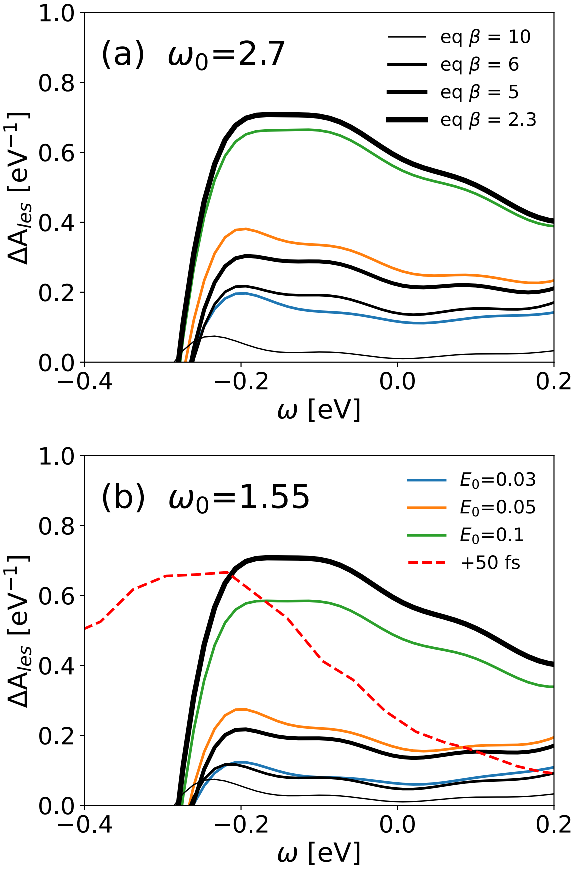

FIG. 7. Difference in the occupation from the equilibrium value for $\beta = 12$ eV^{-1}. The nonequilibrium distributions are measured at time $t = 17$ fs for a pulse with $\omega_0 = 2.7$ eV (a) and 1.55 eV (b). In panel (b), the dashed line shows experimental data extracted from Fig. 2(b) of Ref. [8] (with an arbitrary rescaling factor) for comparison.

atomic configurations in equilibrium, and in determining the energy absorption from an optical pulse.

While the experimentally measured photoinduced metal states may be nonthermal in the sense of different electronic and lattice temperatures, our analysis does not provide any clear indication for the existence of a long-lived photoinduced nonequilibrium metallic state of the electronic subsystem in Cr-doped V_2O_3. This is in contrast to the situation found in photodoped VO_2 [7], where the simpler and sparser energy level structure leads to distinctly nonthermal metal states that last for hundreds of fs.

The simulations presented in this work assumed a homogeneous system, with the Cr doping merely affecting the lattice structure. As discussed in Ref. [16], in practice, the Cr-doping could produce "condensation nuclei" and create isolated insulating islands around the Cr impurities. The possible role of inhomogeneities on the excitation and relaxation pathway in $(V_{1-x}Cr_x)_2O_3$ ($x = 0.038$) is an interesting topic for future studies.

ACKNOWLEDGMENTS

This work was supported by the Swiss National Science Foundation via the Research Unit QUAST of Deutsche Foschungsgemeinschaft (FOR5249) (J.C.). The calculations were run on the beo05 cluster at the University of Fribourg, using a code based on NESSi [44].

---

[1] M. Ligges, I. Avigo, D. Golež, H. U. R. Strand, Y. Beyazit, K. Hanff, F. Diekmann, L. Stojchevska, M. Kalläne, P. Zhou, K. Rossnagel, M. Eckstein, P. Werner, and U. Bovensiepen, Ultrafast doublon dynamics in photoexcited $1T$-TaS_2, Phys. Rev. Lett. **120**, 166401 (2018).

[2] J. Dong, W. Qi, D. Shin, L. Cario, Z. Chen, R. Grasset, D. Boschetto, M. Weis, P. Lample, E. Pastor, T. Ritschel, M. Marsi, A. Taleb, N. Park, A. Rubio, E. Papalazarou, and L. Perfetti, Dynamics of electronic states in the insulating intermediate surface phase of $1T$-TaS_2, Phys. Rev. B **108**, 155145 (2023).

[3] F. Petocchi, C. W. Nicholson, B. Salzmann, D. Pasquier, O. V. Yazyev, C. Monney, and P. Werner, Mott versus hybridization gap in the low-temperature phase of $1T$-TaS_2, Phys. Rev. Lett. **129**, 016402 (2022).

[4] F. Petocchi, J. Chen, J. Li, M. Eckstein, and P. Werner, Photoinduced charge dynamics in $1T$-TaS_2, Phys. Rev. B **107**, 165102 (2023).

[5] V. R. Morrison, R. P. Chatelain, K. L. Tiwari, A. Hendaoui, A. Bruhács, M. Chaker, and B. J. Siwick, A photoinduced metal-like phase of monoclinic VO_2 revealed by ultrafast electron diffraction, Science **346**, 445 (2014).

[6] D. Wegkamp, M. Herzog, L. Xian, M. Gatti, P. Cudazzo, C. L. McGahan, R. E. Marvel, R. F. Haglund, A. Rubio, M. Wolf, and J. Stähler, Instantaneous band gap collapse in photoexcited monoclinic VO_2 due to photocarrier doping, Phys. Rev. Lett. **113**, 216401 (2014).

[7] J. Chen, F. Petocchi, V. Christiansson, and P. Werner, Nature of the photoinduced metallic state in monoclinic VO_2, Phys. Rev. B **109**, L201101 (2024).

[8] G. Lantz, B. Mansart, D. Grieger, D. Boschetto, N. Nilforoushan, E. Papalazarou, N. Moisan, L. Perfetti, V. L. R. Jacques, D. Le Bolloc'h, C. Laulhé, S. Ravy, J.-P. Rueff, T. E. Glover, M. P. Hertlein, Z. Hussain, S. Song, M. Chollet, M. Fabrizio, and M. Marsi, Ultrafast evolution and transient phases of a prototype out-of-equilibrium Mott–Hubbard material, Nat. Commun. **8**, 13917 (2017).

[9] D. Babich, Electron-lattice coupling at the Mott transition driven by electric and/or by light pulse, Thesis, Nantes Université, 2020.

[10] K. Held, G. Keller, V. Eyert, D. Vollhardt, and V. I. Anisimov, Mott-Hubbard metal-insulator transition in paramagnetic V_2O_3: An LDA+DMFT(QMC) study, Phys. Rev. Lett. **86**, 5345 (2001).

[11] G. Keller, K. Held, V. Eyert, D. Vollhardt, and V. I. Anisimov, Electronic structure of paramagnetic V_2O_3: Strongly correlated metallic and Mott insulating phase, Phys. Rev. B **70**, 205116 (2004).

[12] M. S. Laad, L. Craco, and E. Müller-Hartmann, Orbital-selective insulator-metal transition in V_2O_3 under external pressure, Phys. Rev. B **73**, 045109 (2006).

[13] A. I. Poteryaev, J. M. Tomczak, S. Biermann, A. Georges, A. I. Lichtenstein, A. N. Rubtsov, T. Saha-Dasgupta, and O. K. Andersen, Enhanced crystal-field splitting and orbital-selective coherence induced by strong correlations in V_2O_3, Phys. Rev. B **76**, 085127 (2007).

[14] A. Toschi, P. Hansmann, G. Sangiovanni, T. Saha-Dasgupta, O. K. Andersen, and K. Held, Spectral properties of the Mott Hubbard insulator $(Cr_{0.011}V_{0.989})_2O_3$ calculated by LDA+DMFT, J. Phys.: Conf. Ser. **200**, 012208 (2010).

[15] F. Rodolakis, P. Hansmann, J.-P. Rueff, A. Toschi, M. W. Haverkort, G. Sangiovanni, A. Tanaka, T. Saha-Dasgupta, O. K. Andersen, K. Held, M. Sikora, I. Alliot, J.-P. Itié, F. Baudelet, P. Wzietek, P. Metcalf, and M. Marsi, Inequivalent routes across the Mott transition in V_2O_3 explored by x-ray absorption, Phys. Rev. Lett. **104**, 047401 (2010).

[16] P. Hansmann, A. Toschi, G. Sangiovanni, T. Saha-Dasgupta, S. Lupi, M. Marsi, and K. Held, Mott–Hubbard transition in V_2O_3 revisited, Phys. Status Solidi B **250**, 1251 (2013).

[17] D. B. McWhan, T. M. Rice, and J. P. Remeika, Mott transition in Cr-doped V_2O_3, Phys. Rev. Lett. **23**, 1384 (1969).

[18] D. B. McWhan and J. P. Remeika, Metal-insulator transition in $(V_{1-x}Cr_x)_2O_3$, Phys. Rev. B **2**, 3734 (1970).

[19] D. B. McWhan, A. Menth, J. P. Remeika, W. F. Brinkman, and T. M. Rice, Metal-insulator transitions in pure and doped V_2O_3, Phys. Rev. B **7**, 1920 (1973).

[20] P. D. Dernier, The crystal structure of V_2O_3 and $(V_{0.962}Cr_{0.038})_2O_3$ near the metal-insulator transition, J. Phys. Chem. Solids **31**, 2569 (1970).

[21] W. R. Robinson, High-temperature crystal chemistry of V_2O_3 and 1% chromium-doped V_2O_3, Acta Crystallogr. Sect. B **31**, 1153 (1975).

[22] S. Lupi, L. Baldassarre, B. Mansart, A. Perucchi, A. Barinov, P. Dudin, E. Papalazarou, F. Rodolakis, J.-P. Rueff, J.-P. Itié,

S. Ravy, D. Nicoletti, P. Postorino, P. Hansmann, N. Parragh, A. Toschi, T. Saha-Dasgupta, O. K. Andersen, G. Sangiovanni, K. Held *et al.*, A microscopic view on the Mott transition in chromium-doped V_2O_3, Nat. Commun. **1**, 105 (2010).

[23] J.-H. Park, L. H. Tjeng, A. Tanaka, J. W. Allen, C. T. Chen, P. Metcalf, J. M. Honig, F. M. F. de Groot, and G. A. Sawatzky, Spin and orbital occupation and phase transitions in V_2O_3, Phys. Rev. B **61**, 11506 (2000).

[24] W. Kohn and L. J. Sham, Self-consistent equations including exchange and correlation effects, Phys. Rev. **140**, A1133 (1965).

[25] A. Georges, G. Kotliar, W. Krauth, and M. J. Rozenberg, Dynamical mean-field theory of strongly correlated fermion systems and the limit of infinite dimensions, Rev. Mod. Phys. **68**, 13 (1996).

[26] T. Saha-Dasgupta, O. K. Andersen, J. Nuss, A. I. Poteryaev, A. Georges, and A. I. Lichtenstein, Electronic structure of V_2O_3: Wannier orbitals from LDA-*N*MTO calculations, arXiv:0907.2841.

[27] B. Mansart, D. Boschetto, S. Sauvage, A. Rousse, and M. Marsi, Mott transition in Cr-doped V_2O_3 studied by ultrafast reflectivity: Electron correlation effects on the transient response, Europhys. Lett. **92**, 37007 (2010).

[28] H. Aoki, N. Tsuji, M. Eckstein, M. Kollar, T. Oka, and P. Werner, Nonequilibrium dynamical mean-field theory and its applications, Rev. Mod. Phys. **86**, 779 (2014).

[29] P. Giannozzi, O. Andreussi, T. Brumme, O. Bunau, M. B. Nardelli, M. Calandra, R. Car, C. Cavazzoni, D. Ceresoli, M. Cococcioni, N. Colonna, I. Carnimeo, A. D. Corso, S. de Gironcoli, P. Delugas, R. A. DiStasio, A. Ferretti, A. Floris, G. Fratesi, G. Fugallo *et al.*, Advanced capabilities for materials modelling with QUANTUM ESPRESSO, J. Phys.: Condens. Matter **29**, 465901 (2017).

[30] G. Pizzi, V. Vitale, R. Arita, S. Blügel, F. Freimuth, G. Géranton, M. Gibertini, D. Gresch, C. Johnson, T. Koretsune, J. Ibañez-Azpiroz, H. Lee, J.-M. Lihm, D. Marchand, A. Marrazzo, Y. Mokrousov, J. I. Mustafa, Y. Nohara, Y. Nomura, L. Paulatto *et al.*, WANNIER90 as a community code: New features and applications, J. Phys.: Condens. Matter **32**, 165902 (2020).

[31] F. Aryasetiawan, M. Imada, A. Georges, G. Kotliar, S. Biermann, and A. I. Lichtenstein, Frequency-dependent local interactions and low-energy effective models from electronic structure calculations, Phys. Rev. B **70**, 195104 (2004).

[32] K. Nakamura, Y. Yoshimoto, Y. Nomura, T. Tadano, M. Kawamura, T. Kosugi, K. Yoshimi, T. Misawa, and Y. Motoyama, RESPACK: An *ab initio* tool for derivation of effective low-energy model of material, Comput. Phys. Commun. **261**, 107781 (2021).

[33] C. Friedrich, S. Blügel, and A. Schindlmayr, Efficient implementation of the *GW* approximation within the all-electron FLAPW method, Phys. Rev. B **81**, 125102 (2010).

[34] M. Eckstein and P. Werner, Nonequilibrium dynamical mean-field simulation of inhomogeneous systems, Phys. Rev. B **88**, 075135 (2013).

[35] F. Petocchi, S. Beck, C. Ederer, and P. Werner, Hund excitations and the efficiency of Mott solar cells, Phys. Rev. B **100**, 075147 (2019).

[36] H. Keiter and J. C. Kimball, Diagrammatic approach to the anderson model for dilute alloys, J. Appl. Phys. **42**, 1460 (1971).

[37] M. Eckstein and P. Werner, Nonequilibrium dynamical mean-field calculations based on the noncrossing approximation and its generalizations, Phys. Rev. B **82**, 115115 (2010).

[38] L. de' Medici, J. Mravlje, and A. Georges, Janus-faced influence of Hund's rule coupling in strongly correlated materials, Phys. Rev. Lett. **107**, 256401 (2011).

[39] D. H. Dunlap and V. M. Kenkre, Dynamic localization of a charged particle moving under the influence of an electric field, Phys. Rev. B **34**, 3625 (1986).

[40] N. Tsuji, T. Oka, P. Werner, and H. Aoki, Dynamical band flipping in fermionic lattice systems: An ac-field-driven change of the interaction from repulsive to attractive, Phys. Rev. Lett. **106**, 236401 (2011).

[41] At higher energies, around ≈0.3 eV the theoretical occupations show an upturn associated with the upper Hubbard band, which is not evident in the measured spectra.

[42] P. B. Allen, Theory of thermal relaxation of electrons in metals, Phys. Rev. Lett. **59**, 1460 (1987).

[43] N. Singh, Two-temperature model of nonequilibrium electron relaxation: A review, Int. J. Mod. Phys. B **24**, 1141 (2010).

[44] M. Schüler, D. Golež, Y. Murakami, N. Bittner, A. Herrmann, H. U. R. Strand, P. Werner, and M. Eckstein, NESSi: The non-equilibrium systems simulation package, Comput. Phys. Commun. **257**, 107484 (2020).